Journal of Applied Geophysics (Cairo) Vol. 21, Issu.2, September (2022) (p.p., 28-43)

ISSN: 1687-1251

Egyptian Society of Applied Petrophysics

Journal of Applied Geophysics (Cairo)

Journal home page: https://jag.journals.ekb.eg/

Original Article

An Efficient Inversion Algorithm for interpreting Gravity Data: Different Cases for Mineral Resources Development

Mahmoud Elhussein[1]*, Neil Anderson [2]

[1] *Department of Geophysics, Faculty of Science, Cairo University, P.O. 12613, Giza, Egypt.*

[2] *Department of Geosciences and Geological and Petroleum Engineering, Missouri University of Science and Technology.*

ARTICLE INFO

Keywords:
Mining
Gravity
PSO
Thin sheet
Depth.

Received: 2 May 2022;
Revised: 10 July 2022
Accepted: 12 August 2022
Published: 1 September, 2022.

ABSTRACT

The gravity method is one of the most useful mining-applicable approaches because many economic minerals are denser than their host rock. In this study, an efficient processing technique was developed and applied to invert both the synthetic gravity data generated for three thin dipping mineralized sheets of finite depth extent (with and without noises) and two dipping sheets of mineral deposits of gravity datasets from Canada and Cuba, respectively. The technique employed relies upon global particle-swarm-optimization (PSO) technique, which was used, to determine the characteristic parameters of the thin dipping sheets, including the amplitude coefficient, the depth to the upper edge, depth to the lower edge, angle of dip and the source origin (w). The processing outputs support the conclusion that, the PSO technique is fast, accurate and effective, and applicable to the noisy data. The inverted gravity data from both Canada and Cuba are mostly consistent with the available borehole control.

* Corresponding author at: *E-mail:* melhussein@cu.edu.eg

1. Introduction

The geophysical gravity technique is a potential field geophysical tool, used to map and model variations in the earth's gravitational field (Essa and Elhussein, 2018). The gravity method is routinely used to image the subsurface in support of a variety of investigations, including mineral and hydrocarbon prospecting, as well as archaeological, geotechnical, geologic, hydro-geologic, geothermal and environmental assessments, as shown by the studies of (Davis et al., 1957; Roy, 1966; Nettleton, 1976; Roy et al., 2000; Elawadi et al., 2004; Fedi, 2007; Hinze et al., 2013; Essa and Elhussein, 2018; Essa et al., 2018; and Essa and Munschy, 2019).

The gravity method is considered limited, because of its ill-posedness and non-uniqueness issues. Various innovative inversion methods have been developed, to overcome these two potential problems, with the objective of accurately determining the parameters of causative bodies including the source origin position, amplitude factor, depth and dip angle (Zhdanov, 2002; Tarantola, 2005; Essa and Elhussein, 2018; and Essa and Munschy, 2019). These inversion methods include the Fourier-transform technique (Odegard and Berg, 1965; Sharma and Geldart, 1968; and Chacko and Bhattacharya 1980), the 3-D Euler-deconvolution technique (Thompson, 1982; Zhang et al., 2000; and Ghosh, 2016), the least-squares optimization technique (Gupta, 1983; Abdelrahman et al., 1991; Abdelrahman and Sharafeldin, 1995; Abdelrahman et al., 2003; Essa, 2014; and Abdelrahman and Essa, 2015), the simple characteristic points, master curves and nomograms (Grant and West, 1965; Rao et al., 1986; Kara and Kanli, 2005; and Essa 2007 and 2012), the moving-average inversion technique (Abdelrahman et al., 2006; and Essa, 2013), the gradient technique (Saad, 2006), 2-D, 2.5-D and 3-D modelling (Bhaskara Rao et al., 1990; Pinto and Casas, 1996; Zhang et al., 2001; and Eshaghzadeh, 2018); and the fair functions technique (Asfahani and Tlas, 2012). Unfortunately, most of these techniques have their own issues. Some techniques require the input of priori geological information. Others are of few data points dependent or require the accurate separation of the residual anomaly. Problems related to these issues can result in the spatial shifting of the calculated model and error in the determined parameters (Essa and Elhussein, 2018; and Essa and Munschy, 2019). More recently, gravity inversion techniques, which rely upon the artificial intelligence (like simulated annealing) have been developed (Sen and Stoffa, 2013; Biswas, 2015; and Biswas, 2016), PSO (Singh and Biswas, 2016; Essa and Elhussein, 2018; and Essa and Munschy, 2019), neural-network (Osman et al., 2006; and Al-Garni, 2013).

In this work, a PSO algorithm was developed and applied for inverting the gravity datasets for the three thin dipping mineralized sheets of finite depth and to estimate the sheet parameters, including the amplitude coefficient (Ac), depth to the upper edge (h), depth to the lower edge (d), angle of dip (β) and the source origin (w). The PSO technique was also applied to noiseless synthetic models, and noisy models with different random Gaussian noise levels, 10 % and 20 % random noises, and the two mining case studies from Canada and Cuba.

2. Methodology

2.1. Forward modelling

The gravity anomaly (Δg), as expressed by the dipping thin sheet of finite depth, at any point (x_i), is given by (Rao and Murthy, 1978; Sinha and Babu 1985) (Fig. 1):

$$\Delta g(x_i) = A_c \left\{ \frac{1}{2}\sin(\beta)\, ln \frac{((x_i - w) - a)^2 + d^2}{(x_i - w)^2 + h^2} + \cos(\beta) \left[tan^{-1}\left(\frac{x_i - w}{h}\right) - tan^{-1}\left(\frac{(x_i - w) - a}{d}\right)\right]\right\},$$
$$i = 0, 1, 2, 3, \dots\dots\dots\dots, M \qquad (1)$$

M represents the data points number; A_c represents the amplitude coefficient (mGal), which given by: $2G\Delta\sigma t$, where: G represents universal gravitational constant ($cm^3.g^{-1}.s^{-2}$), $\Delta\sigma$ represents the difference between the source's density and surrounding's density ($g.cm^{-3}$) and t is the structure's thickness (dipping thin sheet); h is the upper edge depth of the structure (m); d is the lower edge depth of the structure (m); w represents the position of the structure body (m); β represents the structure dip angle (degree) and a is given by $\left[\frac{d-h}{tan\beta}\right]$.

2.2. Inversion technique

Inversion technique used in this work is dependent upon global PSO algorithm, the development of this technique was done by Eberhart and Kennedy (1995) in the late twentieth century. More recently, this algorithm was modified to be utilized in multi-discipline geophysical applications (Sen and Stoffa, 2013; Essa and Elhussein, 2018; Essa and Munschy, 2019; and Essa and Elhussein, 2020). The nature of PSO-inversion algorithm is stochastic; the algorithm can be explained by considering an example of birds group looking for food. In this example, each bird represents a model. For each model, there are two vectors: the location and velocity. The value of parameter represents location vector. The initiation of swarm starts with a random model using different variable ranges. The positions and velocities of various particles are iteratively updated using the following formulae:

$$x_i^{k+1} = x_i^k + V_i^{k+1}, \qquad (2)$$

$$V_i^{k+1} = c_3 V_i^k + c_1 rand1\left(T_{best} - x_i^{k+1}\right) + c_2 rand2\left(J_{best} - x_i^{k+1}\right), \qquad (3)$$

where: x_i^k and V_i^k are the location and the velocity of the i^{th} particle respectively at the k^{th} iteration; *rand1* and *rand2* for random values ranging from 0 to 1; c_1 *and* c_2 are coefficients called cognitive and social respectively, take the value 2 (Parsopoulos and Vrahatis, 2002; Singh and Biswas, 2016; Essa and Munschy, 2019; Essa and Elhussein, 2020; and Elhussein, 2020); c_3 represents the factor of inertia, that balances the velocity of model, its value is less than 1; T_{best} represents the best location that the individual model can achieve and J_{best} represents the best global position that any model reach in the swarm. During each iteration, both location and speed of each model are updated. When convergence is reached (the objective function is optimized), the iteration process ends (Venter and Sobieski, 2002; and Essa and Elhussein 2020).

2.2. Inversion technique

Inversion technique used in this work is dependent upon global PSO algorithm, the development of this technique was done by Eberhart and Kennedy (1995) in the late twentieth century.

More recently, this algorithm was modified to be utilized in multi-discipline geophysical applications (Sen and Stoffa, 2013; Essa and Elhussein, 2018; Essa and Munschy, 2019; and Essa and Elhussein, 2020). The nature of PSO-inversion algorithm is stochastic; the algorithm can be explained by considering an example of birds group looking for food. In this example, each bird represents a model. For each model, there are two vectors: the location and velocity. The value of parameter represents location vector. The initiation of swarm starts with a random model using different variable ranges. The positions and velocities of various particles are iteratively updated using the following formulae:

$$x_i^{k+1} = x_i^k + V_i^{k+1}, \qquad (2)$$

$$V_i^{k+1} = c_3 V_i^k + c_1 rand1\left(T_{best} - x_i^{k+1}\right) + c_2 rand2\left(J_{best} - x_i^{k+1}\right), \qquad (3)$$

where: x_i^k and V_i^k are the location and the velocity of the i^{th} particle respectively at the k^{th} iteration; *rand1* and *rand2* for random values ranging from 0 to 1; c_1 *and* c_2 are coefficients called cognitive and social respectively, take the value 2 (Parsopoulos and Vrahatis, 2002; Singh and Biswas, 2016; Essa and Munschy, 2019; Essa and Elhussein, 2020; and Elhussein, 2020); c_3 represents the factor of inertia, that balances the velocity of model, its value is less than 1; T_{best} represents the best location that the individual model can achieve and J_{best} represents the best global position that any model reach in the swarm. During each iteration, both location and speed of each model are updated. When convergence is reached (the objective function is optimized), the iteration process ends (Venter and Sobieski, 2002; and Essa and Elhussein 2020).

The best global solution (J_{best}) is achieved, by optimizing the objective function (ψ_{obj}) given by the following equation, using iterations.

$$\psi_{obj} = \frac{1}{M}\sum_{i=1}^{M}[\Delta g^O(x_i) - \Delta g^C(x_i)]^2. \qquad (4)$$

M represents the data points, Δg^O represents the measured gravity and Δg^C represents the estimated gravity.

The various sources parameters $(A_c, h, d, \beta$ and $w)$ are estimated by minimizing equation (4). The RMS (root mean square) error is calculated, using the following formula after estimating the source parameters:

$$RMS = \sqrt{\frac{1}{M}\sum_{i=1}^{M}[\Delta g^O(x_i) - \Delta g^C(x_i)]^2}\ . \qquad (5)$$

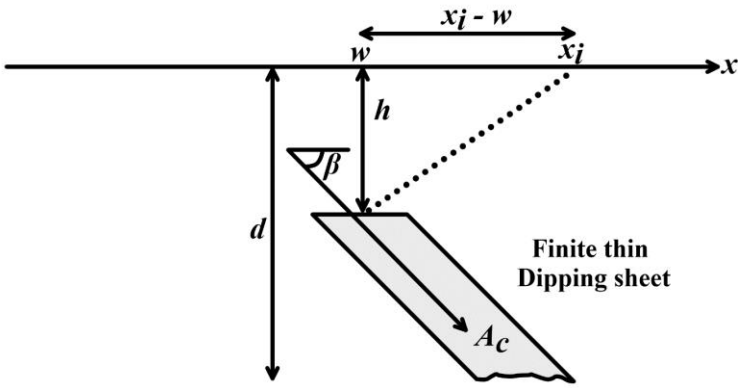

Fig. 1. Geometric structures for dipping thin sheet of finite depth extent.

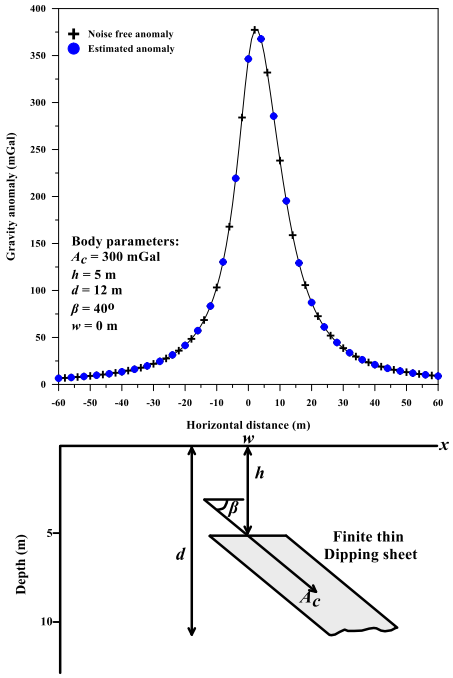

Fig. 2. A synthetic noiseless gravity anomaly caused by dipping thin sheet of finite depth model using these parameters: A_c = 300 mGal, h = 5 m,

3. Synthetic models

3.1. First synthetic example

A gravity anomaly, generated for a finite depth extent dipping thin sheet, using the following parameters: anomaly profile length = 120 m, A_c = 300 mGal, h = 5 m, d = 12 m, β = 40º and w = 0 m (Fig. 2). Then the developed PSO-technique was applied to this gravity anomaly profile, for estimating the dipping sheet parameters (Table 1). Table (1) represents the calculated structure parameters (A_c, h, d, β and w), the error of A_c, h, d and β are 0 % and the error of RMS is 0 mGal. The comparison between the noiseless profile and the calculated profile is demonstrated in Fig. 2.

For the purpose of testing the efficiency of PSO-technique, in the presence of noise, the above synthetic data were contaminated with random Gaussian noises levels of both 10 % and 20 % (Fig.s 3 and 4) respectively. The PSO-technique was used to compute the model parameters (Table 1). The calculated parameters for the 10% noise example are: ($A_c = 310.29$ mGal , $h = 4.9\, m, d = 11.9\, m, \beta = 39.18^o$ and $w = -0.12\, m$); while the error estimates of A_c, h, d *and* β are 3.43 %, 2 %, 0.83 % and 2.05 %, respectively, and the RMS error calculated is 2.85 mGal. The estimated parameters for the 20% noises example are: $A_c = 288.20$ mGal , $h = 5.1\, m, d = 11.9\, m, \beta = 40.68^o$ and $w = 0.15\, m$; while the error estimates of A_c, h, d *and* β are 3.93 %, 2 %, 0.83 % and 1.7 %, respectively, and the RMS error calculated is 3.74 mGal (Table 1). Fig.s 3 and 4 show the comparison between the 10% noisy gravity profile and the computed profile and the 20% noisy profile and the computed one, respectively.

Table 1. Computed results of Global PSO-optimization technique applied to gravity profile (120 m) due to dipping thin sheet of finite depth (A_c = 300 mGal, h = 5 m, d = 12 m, β = 40o and w = 0 m), with and without various noise levels of 10 % and 20 % random Gaussian noise.

Parameters	Used ranges	Results	Error (%)	RMS error (mGal)
Noise-free data				
A_c (mGal)	50 – 800	300	0	0
h (m)	1 – 20	5	0	
d (m)	3 – 30	12	0	
β (degree)	20 – 80	40	0	
w (m)	-10 – 10	0	--------	
with 10 % random noise				
A_c (mGal)	50 – 800	310.29	3.43	2.85
h (m)	1 – 20	4.90	2	
d (m)	3 – 30	11.90	0.83	
β (degree)	20 – 80	39.18	2.05	
w (m)	-10 – 10	-0.12	--------	
with 20% random noise				
A_c (mGal)	50 – 800	288.20	3.93	3.74
h (m)	1 – 20	5.1	2	
d (m)	3 – 30	11.9	0.83	
β (degree)	20 – 80	40.68	1.7	
w (m)	-10 – 10	0.15	--------	

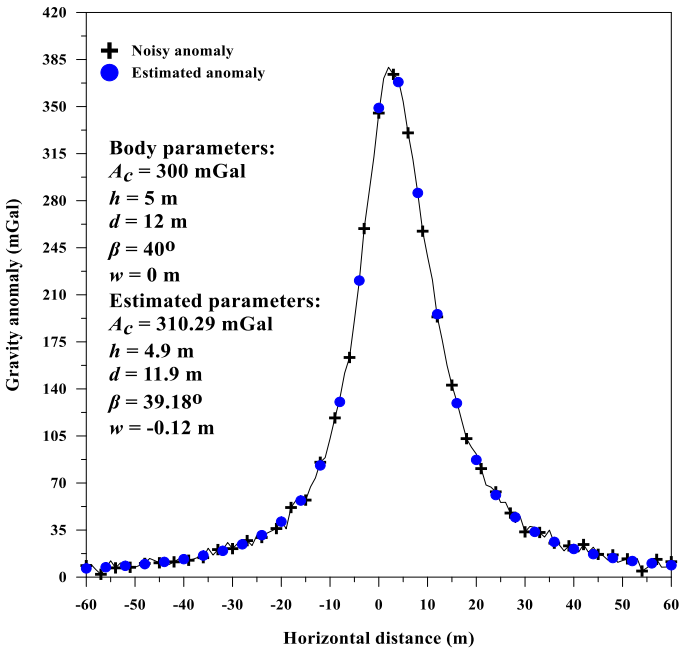

Fig. 3. A gravity profile mentioned in Figure 2 with a 10 % random noise and the estimated anomaly.

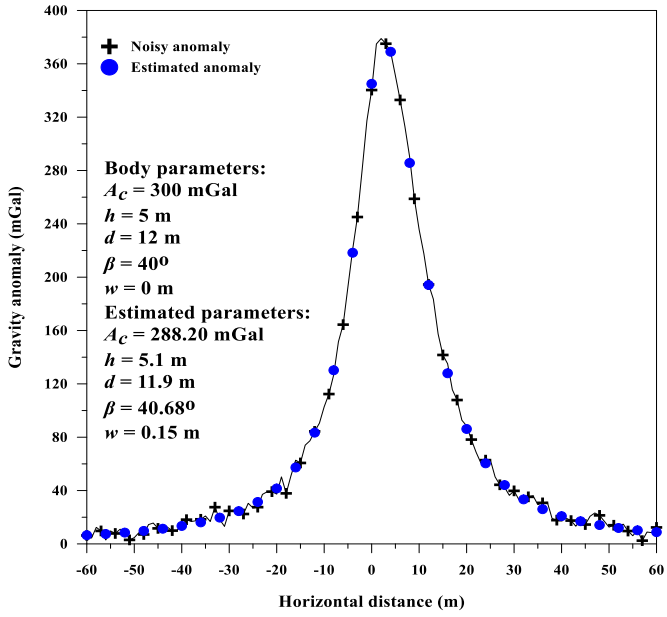

Fig. 4. A gravity profile mentioned in Figure 2 with a 20 % random noise and the estimated anomaly.

3.2. Second synthetic example

To examine the efficiency of the PSO technique in case of a proximal structure, generating its own gravity anomaly, the technique was applied to a composite anomaly. The composite anomaly was generated by a dipping thin sheet of finite depth extent (main target), with the following parameters: A_c = 400 mGal, h = 4 m, d = 10 m, β = 45° and w = 0 m, and a proximal sphere, using these parameters: A_c = 4000 mGal.m^2, z (depth) = 5 m, q (shape factor) = 1.5, w = 30 m and 120 m for profile length (Fig. 5). The composite gravity anomaly can be represented by the following formula:

$$\Delta g_{comp}(x_i) = 400\left\{\frac{1}{2}\sin(45^o)\, ln\frac{(x_i-a)^2+100}{{x_i}^2+16} + \cos(45^o)\left(tan^{-1}\left(\frac{x_i}{4}\right) - tan^{-1}\left(\frac{x_i-a}{10}\right)\right)\right\} + 4000\left[\frac{5}{((x_i-30)^2+25)^{1.5}}\right], \quad i = 0,1,2,3,\dots\dots\dots,M \qquad (6)$$

We applied the global PSO-technique to the above composite anomaly to compute the thin sheet parameters, by using different parameter's ranges (Table 2). Table (2) represents the estimated parameters ($A_c =$ 425.32 mGal , $h = 3.7\ m, d = 10.7\ m, \beta =$ 47.34° and $w = -0.01\ m$), where the errors of $A_c, h, d\ and\ \beta$ are 6.33 %, 7.50 %, 7 % and 5.2 %, respectively, and the error of RMS is 34.55 mGal. Figure 5 illustrates the comparison between the composite and computed profiles.

3.3. Third synthetic example

For assessing the accuracy and applicability of PSO algorithm, in case of choosing different origins, the optimization algorithm was applied to a 120 m gravity profile caused by finite depth dipping thin sheet, using A_c = 200 mGal, h = 3 m, d = 8 m, β = 65o and w = 20 m (Fig. 6). Table 3 represents the computed parameters (A_c,h,d,β and w), the A_c,h,d,β and w errors are 0 % and the error of RMS is 0 mGal. The comparison between the noiseless profile and the estimated one is illustrated in Figure 6.

Field gravity data are contaminated with noises. To assess the utility of the PSO technique, when applied to noisy gravity data, the third synthetic example was contaminated with different random Gaussian noises levels of 10% and 20% (Fig. 7 & 8), respectively). The PSO-technique was applied to both noisy data and the different parameters were computed (Table 3). Table (3) represents the computed parameters

($A_c =$ 210 mGal , $h = 3\ m, d = 7.9\ m, \beta =$ 62.97° and $w =$ 19.92 m),

where the error of A_c, h, d, β and w are 5 %, 0 %, 1.25 %, 3.12 % and 0.4 %, respectively, and 2.55 mGal RMS error in case of 10 % noisy anomaly. In case of using 20 % random Gaussian noises, the estimated parameters are: $A_c =$ 210 mGal , $h = 3.2\ m, d = 7.6\ m, \beta =$ 68.48° and $w =$ 20.20 m and the error of A_c, h, d, β and w are 5 %, 6.67 %, 5 %, 5.35 % and 1 %, respectively, and 3.28 mGal RMS error (Table 1). Fig. 7 & 8 show the difference between the 10 % noisy profile and the estimated profile and 20 % noisy profile and the computed one respectively anomaly, respectively.

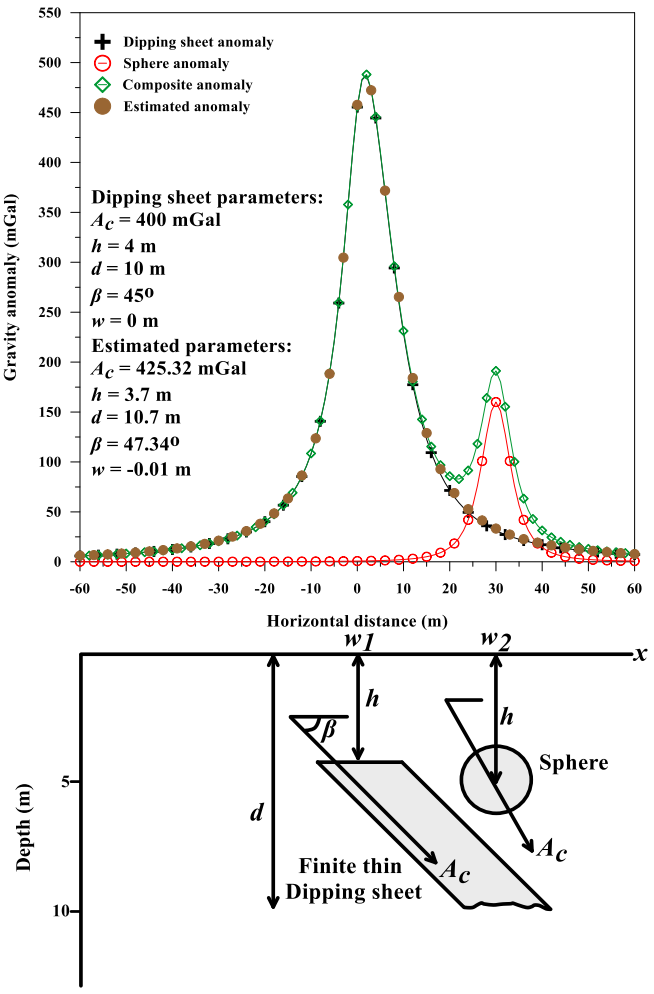

Fig.5. A composite gravity profile of finite depth dipping thin sheet with (A_c = 400 mGal, h = 4 m, d = 10 m, β = 45o and w = 0 m) and sphere (A_c = 4000 mGal.m2, z = 5 m, q = 1.5, w = 30 m and 120 m profile length; and the estimated anomaly.

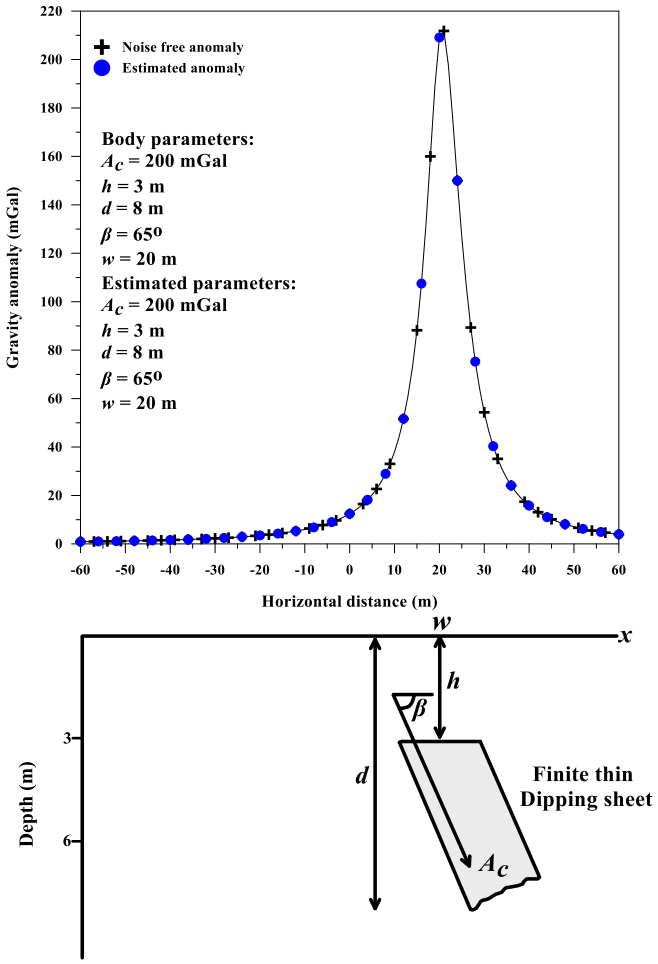

Fig. 6. A 120 m synthetic noise free gravity anomaly profile due to dipping thin sheet of finite depth using: A_c = 200 mGal, h = 3 m, d = 8 m, β = 65o and w = 20 m, and 120 m profile length; and the computed anomalv.

Table 2. Computed results of Global PSO-optimization technique applied to composite anomaly of dipping thin sheet with finite depth (A_c = 400 mGal, h = 4 m, d = 10 m, β = 45o and w = 0 m) and sphere model (A_c = 4000 mGal.m2, z = 5 m, q = 1.5 and w = 30 m).

Parameters	Used ranges	Results	Error (%)	RMS error (mGal)
A_c (mGal)	100 – 1500	425.32	6.33	34.55
h (m)	1 – 20	3.7	7.5	
d (m)	3 – 30	10.7	7	
β (degree)	20 – 85	47.34	5.2	
w (m)	-10 – 10	-0.01	---------	

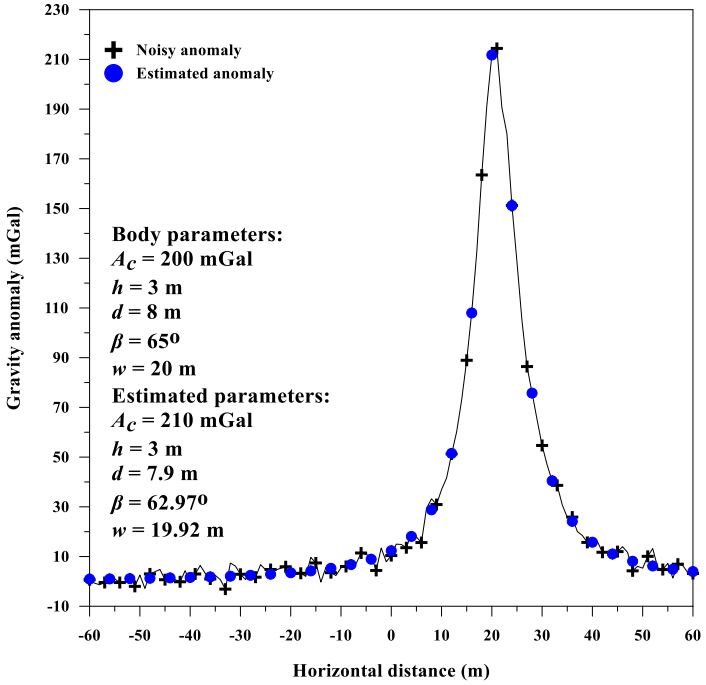

Fig. 7. A gravity profile illustrated in Figure 6 with 10 % random noise and the estimated anomaly.

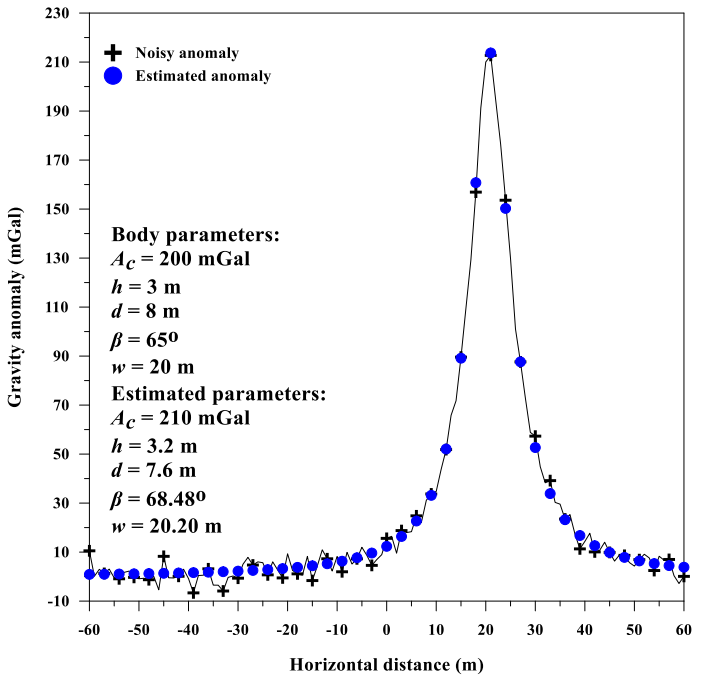

Fig. 8. A gravity anomaly illustrated in Figure 6 with a 20 % random noise impeded and the computed profile.

Table 3. Numerical results of Global PSO-optimization technique applied to gravity profile (120 m) due to dipping thin sheet with finite depth (A_c = 200 mGal, h = 3 m, d = 8 m, β = 65o and w = 20 m), with and without different noise levels of 10 % and 20 % random noise.

Parameters	Used ranges	Results	Error (%)	RMS error (mGal)
Noise-free data				
A_c (mGal)	50 – 800	200	0	0
h (m)	0.5 – 20	3	0	
d (m)	3 – 30	8	0	
β (degree)	20 – 90	65	0	
w (m)	-10 – 40	20	0	
with 10 % random noise				
A_c (mGal)	50 – 800	210	5	2.55
h (m)	0.5 – 20	3	0	
d (m)	3 – 30	7.9	1.25	
β (degree)	20 – 90	62.97	3.12	
w (m)	-10 – 40	19.92	0.4	
with 20 % random noise				
A_c (mGal)	50 – 800	210	5	3.28
h (m)	0.5 – 20	3.2	6.67	
d (m)	3 – 30	7.6	5	
β (degree)	20 – 90	68.48	5.35	
w (m)	-10 – 40	20.20	1	

4. Field examples

To examine the efficiency of the applicability of the PSO technique in mining operations, the algorithm was applied to two real field examples. The first data set is from Canada and the second is from Cuba.

4.1. Mobrun sulfide deposit anomaly, Québec, Canada

In 1954, Rio Canadian Exploration Limited discovered the Mobrun sulfide deposit. The deposit was characterized by a prominent electromagnetic anomaly. The Mobrun mine is located about 34 km northeast of Rouyn-Noranda (Barrett et al., 1992) (Fig. 9). The ore body is composed of two complex massive sulfide lenses (Barrett et al., 1992), of which only one is modeled here.

A residual gravity anomaly profile, extracted from the real field data, was generated for a profile oriented perpendicular to the strike of one of the massive sulfide bodies (Grant and West, 1965; Sivakumar Sinha and Ram Babu, 1985; Roy et al., 2000; and Biswas 2015) (Fig.10). The residual gravity profile length is 292 m; it was sampled at 1 m intervals. The global PSO technique was applied to the residual gravity profile, to estimate the ore body parameters $(A_c, h, d, \beta \text{ and } w)$, using different ranges (Table 4). The calculated parameters are: $A_c = 682 \text{ x } 10^{-3}$ mGal, $h = 28.97$ m, $d = 188.74$ m, $\beta = 84.37^{o}$ and $w = 159.46$ m, and the RMS error is 0.04 mGal (Table 4). The correlation between the measured and computed gravity anomalies is shown in Figure (10). The results obtained from the proposed method is consistent well with the drilling information, which indicates that, the depth to the top of the ore body is 30.48 m and the depth to the bottom is 194 m (Sivakumar Sinha and Ram Babu, 1985; and Roy et al., 2000). Table (5) shows the comparison between the estimated parameters of the present method and these from different methods in the literatures.

4.2. Camaguey chromite area anomaly, Cuba

The chromite deposits of Camaguey area were developed along the contact of serpentinized dunite and peridotite rocks, and feldspathic rocks (Davis et al., 1957). The chromite's gravity data were acquired across the dipping sheet-shaped chromite-bearing ore body by Davis et al. (1957), as a part of an exploration program conducted by the Geological Survey of the United States in the Camaguey district, Cuba.

A 71 m residual gravity anomaly profile was generated along a profile oriented perpendicular to the strike of the chromite deposit (Fig. 11). The profile was sampled at 0.5 m intervals. The global PSO optimization algorithm was applied to the gravity anomaly profile, for estimating different parameters $(A_c, h, d, \beta \text{ and } w)$, using different ranges (Table 6), in which the computed parameters are $A_c = 24 \text{ x } 10^{-2}$ mGal , $h = 10.11$ m, $d = 20.00$ m, $\beta = 94^{o}$ and $w = 41.13$ m, and the RMS error is 6.55 x 10^{-3} mGal (Table 6). The difference between the measured and estimated anomalies is illustrated in Fig.11. The results obtained from the proposed method are matched well with drilling information, which indicated that, the depth to the top is ranging from 3.22 m to 22.86 m and the depth to the bottom is ranging from 12.65 m to 76.20 m (Davis et al., 1957). Table (7) shows the comparison between the computed parameters of the present technique and those from different algorithms in the literatures.

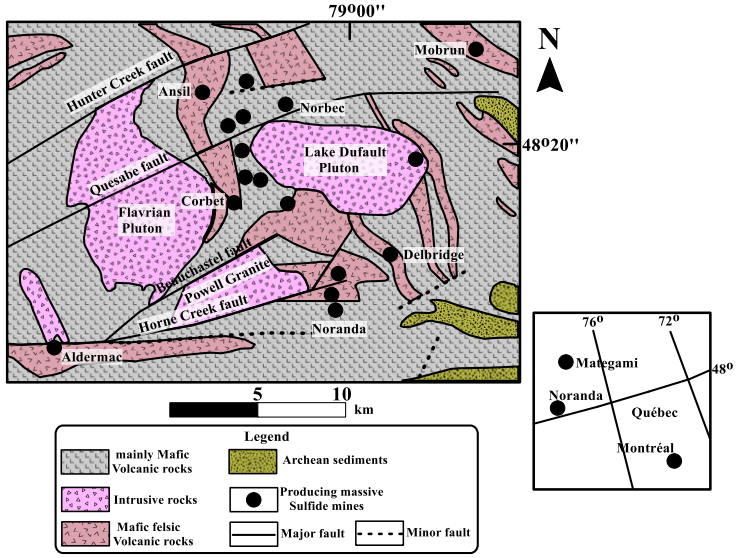

Fig. 9. Geological map of the Mobrun zone, Noranda area, Canada (Modified after Barrett et al. 1992).

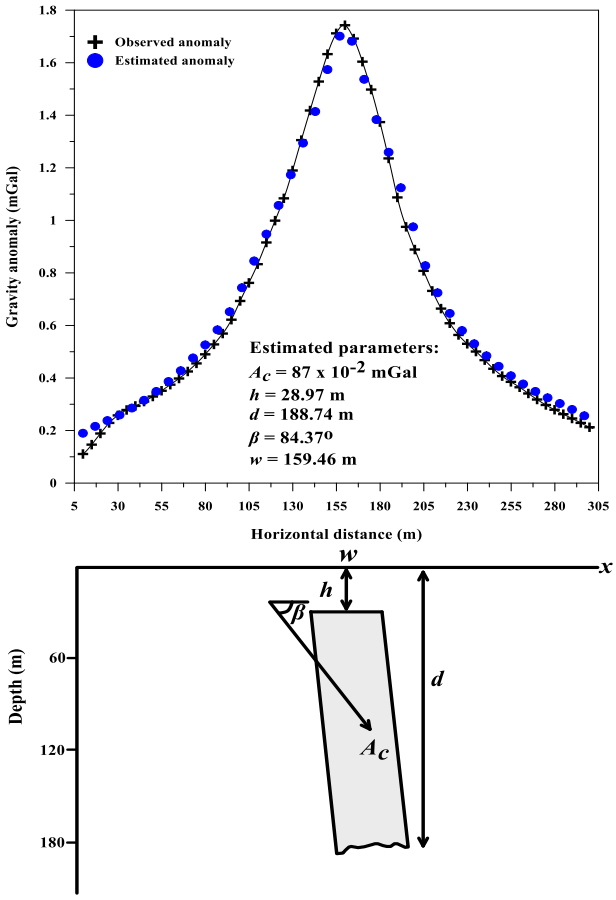

Fig.10. The measured and the computed gravity profile for the Mobrun sulfide deposit anomaly, Québec, Canada field example.

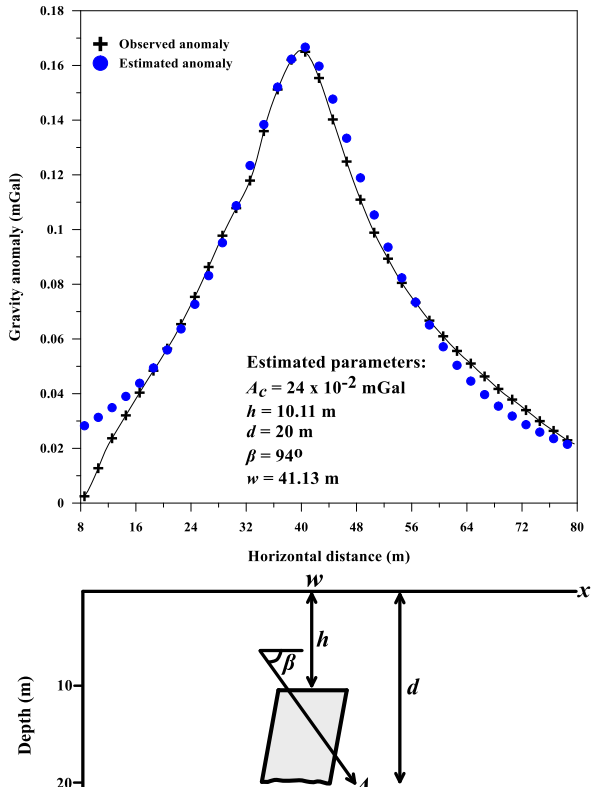

Fig.11. The observed and the estimated gravity anomaly profile for the Camaguey chromite area anomaly, Cuba field example.

Table 4. Computed results of Global PSO-optimization technique applied to the residual gravity profile of Mobrun sulfide deposit anomaly, Québec, Canada.

Parameters	Used ranges	Result	RMS error (mGal)
A_c (mGal)	15 x 10^{-2} – 300 x 10^{-2}	87 x 10^{-2}	0.04
h (m)	10 – 50	28.97	
d (m)	60 – 200	188.74	
β (degree)	20 – 140	84.37	
w (m)	120 – 180	159.46	

Table 5. A comparison between Numerical results computed from various algorithms for the residual gravity profile of Mobrun sulfide deposit anomaly, Québec, Canada.

Methods Parameters	**Grant and West (1965) method**	**Sinha and Babu (1985) method**	**Sinha and Babu (1985) Drilling**	**Roy (2000) method**	**Al-Garni (2018) method**	**Present method**
A_c **(mGal)**	-------	-------	-------	-------	146.37 (arbitrary units)	87 x 10^{-2}
h **(m)**	17.07	24.38	30.48	22.7	28.04	28.97
d **(m)**	-------	-------	193.97	52	-------	188.74
β **(degree)**	83	79	-------	-------	80.51	84.37
w **(m)**	-------	-------	-------	-------	-------	159.46

Table 6. Numerical results of Global PSO-optimization technique applied to the residual gravity anomaly profile of Camaguey chromite area anomaly, Cuba.

Parameters	**Used ranges**	**Results**	**RMS error (mGal)**
A_c **(mGal)**	1 x 10^{-2} – 150 x 10^{-2}	24 x 10^{-2}	6.55 x 10^{-3}
h **(m)**	3 – 50	10.11	
d **(m)**	5 – 80	20.00	
β **(degree)**	20 – 140	94.00	
w **(m)**	28 – 52	41.13	

Table 7. Comparison between Numerical results obtained from various methods for the residual gravity anomaly profile of Camaguey chromite area anomaly, Cuba.

Methods Parameters	Davis et al. (1957) drilling	Mehanee (2014) method	Biswas (2015) method	Mehanee and Essa (2015)	Present method
A_c (mGal)	-------	3 (mGal.m)	3.5 (m Gal.m)	6990 – 7980 (kg/m^2)	24 x 10^{-2}
h (m)	3.22 – 22.86	16	16.2	6 – 7	10.11
d (m)	12.65 – 76.20	-------	-------	-------	20.00
β (degree)	-------	-------	79	94	94.00
w (m)	-------	-------	-1.8	-------	41.13

5. Conclusions

The accuracy and efficiency of the PSO technique was demonstrated, using synthetic data, with and without random Gaussian noises, and real gravity datasets from Canada and Cuba. The PSO technique can be applied to mineral exploration and can be used to determine the ore body parameters, including the amplitude coefficient (Ac), depth to the upper edge (h), depth to the lower edge (d), dip angle (β), and source origin (w) for the mineralized thin dipping sheet of finite depth extent. The results estimated in case of the theoretical and field data indicate that the PSO technique is an effective quantitative gravity data interpretation tool. The global PSO technique is powerful and provides for fast convergence. These applicability and utility of the PSO technique were confirmed by comparing the models generated for real field data with bore hole control.

Declaration of Competing Interest

The authors declare that they have no conflict of interest.

6. References

Abdelrahman, E. M. & Essa, K. S. (2015). Three least-squares minimization approaches to interpret gravity data due to dipping faults. Pure and Applied Geophysics, 172, 427–438.

Abdelrahman, E. M., Abo-Ezz, E. R., Essa, K. S., El-Araby, T. M. & Soliman, K. S. (2006). A least-squares variance analysis method for shape and depth estimation from gravity data. Journal of Geophysics and Engineering, 3, 143–153.

Abdelrahman, E. M., El-Araby, T. M. & Essa, K. S. (2003). Shape and depth solutions from third moving average residual gravity anomalies using the window curves method. Kuwait Journal of Science and Engineering, 30, 95–108.

Abdelrahman, E. M., Bayoumi, A. I. & El-Araby, H. M. (1991). A least-squares minimization approach to invert gravity data. Geophysics, 56, 115–118.

Abdelrahman, E. M. & Sharafeldin, S. M. (1995). A least-squares minimization approach to shape determination from gravity data. Geophysics, 60, 589–590.

Al-Garni, M. A. (2013). Inversion of residual gravity anomalies using neural network. Arabian Journal of Geosciences, 6, 1509–1516.

Al-Garni, M. A. (2018). Mathematical analysis of gravity anomalies due to an infinite sheet-like structure. Arabian Journal of Geosciences, 11:138. DOI. https://doi.org/10.1007/s12517-018-3473-y.

Asfahani, J. & Tlas, M. (2012). Fair function minimization for direct interpretation of residual gravity anomaly profiles due to spheres and cylinders. Pure and Applied Geophysics, 169, 157–165.

Barrett, T. J., Cattalani, S., Hoy, L., Riopel, J. & Lafleur, P. J. (1992). Massive sulfide deposits of the Noranda area, Quebec. IV. The Mobrun mine. Canadian Journal of Earth Sciences. DOI. https://doi.org/ 10.1139/e92-110. 1349–1374.

Bhaskara Rao, D., Prakash, M. J. & Ramesh Babu, N. (1990). 3D and 2 $\frac{1}{2}$ D Modelling of Gravity Anomalies with Variable Density Contrast. Geophysical Prospecting, 38, 411–422.

Biswas, A. (2015). Interpretation of residual gravity anomaly caused by a simple shaped body using very fast simulated annealing global optimization. Geoscience Frontiers, 6, 875–893.

Biswas, A. (2016). Interpretation of gravity and magnetic anomaly over thin sheet-type structure using very fast simulated annealing global optimization technique. Modeling Earth Systems and Environment, 2:30. DOI. https://doi.org/10.1007/s40808-016-0082-1.

Chacko, S. & Bhattacharya, B. (1980). A method for analysing gravity anomalies due to a geologic contact by Fourier transform. Geoexploration, 18, 43–50.

Davis, W. E., Jackson, W. H. & Richter, D. H. (1957). Gravity prospecting for chromite deposits in Camaguey Province, Cuba. Geophysics, XXII(4), 848–869.

Eberhart, R. C. & Kennedy, J. (1995). A new optimizer using particle swarm theory. In Proceedings of the sixth international symposium on micro machine and human science. IEEE service center, Piscataway, NJ, Nagoya, Japan, 39–43.

Elawadi, E., Salem, A. & Ushijima, K. (2004). Detection of cavities and tunnels from gravity data using a neural network. Exploration Geophysics, 32, 204–208.

Elhussein, M. (2020). A Novel Approach to Self-potential Data Interpretation in Support of Mineral Resource Development. Natural Resources Research. DOI. https://doi.org/10.1007/s11053-020-09708-1.

Eshaghzadeh, A. (2018). 2D and 3D Inverse Modeling of the Residual Gravity Field for a Buried Deposit Mass. Conference Proceedings, 24th European Meeting of Environmental and Engineering Geophysics, 1–5.

Essa, K. S. (2007). A simple formula for shape and depth determination from residual gravity anomalies. Acta Geophysica, 55, 182–190.

Essa, K. S. (2012). A fast least-squares method for inverse modeling of gravity anomaly profiles due simple geometric shaped structures. Near surface geoscience, 18th European meeting of environmental and engineering geophysics, Paris, France.

Essa, K. S. (2013). Gravity interpretation of dipping faults using the variance analysis method. Journal of Geophysics and Engineering. DOI. https://doi.org/10.1088/1742-2132/10/1/015003.

Essa, K. S. (2014). New fast least-squares algorithm for estimating the best-fitting parameters of some geometric structures to measured gravity anomalies. Journal of Advanced Research, 5, 57–65.

Essa, K. S. & Elhussein, M. (2018). Gravity data interpretation using new algorithms: A comparative study; In: Gravity-geoscience applications (ed.) Zouaghi Z, Industrial Technology and Quantum Aspect, InTech, Croatia, 226p.

Essa, K. S., Nady, A. G., Mostafa, M. S. & Elhussein, M. (2018). Implementation of potential field data to depict the structural lineaments of the Sinai Peninsula, Egypt. Journal of African Earth Sciences, 147, 43–53.

Essa, K. S. & Munschy, M. (2019). Gravity data interpretation using the particle swarm optimisation method with application to mineral exploration. Journal of Earth System Science, 128:123. DOI. https://doi.org/10.1007/s12040-019-1143-4.

Essa, K. S. & Elhussein, M. (2020). Interpretation of Magnetic Data Through Particle Swarm Optimization: Mineral Exploration Cases Studies. Natural Resources Research, 29(1), 521–537.

Fedi, M. (2007). DEXP: A fast method to determine the depth and the structural index of potential fields sources. Geophysics, 72(1), I1–I11.

Ghosh, G. K. (2016). Interpretation of Gravity Data using 3D Euler Deconvolution, Tilt Angle, Horizontal Tilt Angle and Source Edge Approximation of the North-West Himalaya. Acta Geophysica. DOI. https://doi.org/10.1515/acgeo-2016-0042.

Grant, F. S. & West, G. F. (1965). Interpretation Theory in Applied Geophysics, New York: McGraw- Hill Book Co.

Gupta, O. P. (1983). A least-squares approach to depth determination from gravity data. Geophysics, 48, 357–360.

Hinze, W. J., von Frese, R. R. B. & Saad, A. H. (2013). Gravity and magnetic exploration: principles, practices and applications, Cambridge University Press. USA, New York.

Kara, I. & Kanli, A. I. (2005). Nomograms for Interpretation of Gravity Anomalies of a Vertical Cylinder. Journal of Balkan Geophysical Society, 8(1), 1–6.

Nettleton, L. L. (1976). Gravity and magnetics in oil prospecting, McGraw-Hill Book Co, New York. 464 p.

Odegard, M. E. & Berg, J. W. (1965). Gravity interpretation using the Fourier integral. Geophysics, 30, 424–438.

Osman, O., Albora, A. M. & Ucan, O. N. (2006). A new approach for residual gravity anomaly profile interpretations: Forced neural network (FNN). Annals of Geophysics, 49, 1201–1208.

Parsopoulos, K. E. & Vrahatis, M. N. (2002). Recent approaches to global optimization problems through Particle Swarm Optimization. Natural Computing, 1, 235–306.

Pinto, V. & Casas, A. (1996). An Interactive 2D and 3D Gravity Modeling Program For IBM-Compatible Personal Computers. Computers & Geosciences, 22(5), 535–546

Rao, B. S. R. & Murthy, I. V. R. (1978). Gravity and magnetic methods of prospecting, New Delhi, Arnold Heinemann.

Rao, P., Subrahmanyam, M. & Murthy, S. (1986). Nomograms for direct interpretation of magnetic anomalies due to long horizontal cylinders. Geophysics, 51, 2150–2159.

Roy, A. (1966). The method of continuation in mining geophysical interpretation. Geoexploration, 4, 65–83.

Roy, L., Agarwal, B. N. P. & Shaw, R. K. (2000). A new concept in Euler deconvolution of isolated gravity anomalies. Geophysical Prospecting, 48, 559–575.

Saad, A. H. (2006). Understanding gravity gradients - A tutorial. The Leading Edge. DOI. https://doi.org/10.1190/1.2335167.

Sen, M. K. & Stoffa, P. L. (2013). Global optimization methods in geophysical inversion. Cambridge Publisher, London, 289 pp.

Sharma, B. & Geldart, L. P. (1968). Analysis of gravity anomalies of two-dimensional faults using Fourier transforms. Geophysical Prospecting, 16, 77–93.

Singh, A. & Biswas, A. (2016). Application of global particle swarm optimization for inversion of residual gravity anomalies over geological bodies with idealized geometries. Natural Resources Research, 25, 297–314.

Tarantola, A. (2005). Inverse problem theory and methods for model parameters estimation. Society of Industrial and Applied Mathematics (SIAM), Pennsylvania, 339 pp.

Thompson, D. T. (1982). EULDPH—A new technique for making computer-assisted depth estimates from magnetic data. Geophysics, 47, 31–37.

Venter, G. & Sobieski, J. (2002). Particle Swarm Optimization. AIAA 2002-1235, 43rd AIAA/ASME/ASCE/ AHS/ASC Structures, Structural Dynamics, and Materials Conference, Denver, CO.

Zhang, C., Mushayandebvu, M. F., Reid, A. B., Fairhead, J. D. & Odegard, M. E. (2000). Euler deconvolution of gravity tensor gradient data. Geophysics, 65(2), 512–520.

Zhang, J., Zhong, B., Zhou, X. & Dai, Y. (2001). Gravity anomalies of 2D bodies with variable density contrast. Geophysics, 66, 809–813.

Zhdanov, M. S. (2002). Geophysical inversion theory and regularization problems. Elsevier, Amsterdam, 633 pp.